

Time-dependent viscous electron flow

P. O. Sukhachov^{1,*} and E. V. Gorbar^{2,3}

¹*Department of Physics, Yale University, New Haven, CT 06520, USA*

²*Department of Physics, Taras Shevchenko National University of Kyiv, Kyiv, 03022, Ukraine*

³*Bogolyubov Institute for Theoretical Physics, Kyiv, 03143, Ukraine*

(Dated: July 20, 2021)

A hydrodynamic flow of electrons driven by an oscillating electric field is investigated. It is found that a double-peak profile of the electric current can appear. Such a profile originates from the interplay of viscous and inertial properties of the electron fluid as well as the boundary conditions. The nontrivial profile of the current results in a characteristic stray magnetic field where peaks could also occur in one of the field components. Analytical results are supported by numerical calculations in samples of different geometries such as straight channel, nozzle, and cavity and are found to be qualitatively insensitive to a specific form of the oscillating electric field. In addition, it is shown that nozzle and cavity provide an efficient means to locally enhance or reduce the fluid velocity.

I. INTRODUCTION

Transport properties are among the most fundamental characteristics of any material. Among several transport regimes, the hydrodynamic one draws significant attention. It is realized when the electron-electron interactions dominate over the scatterings of electrons on impurities and phonons. The hydrodynamic regime of charge and heat transport in solids was proposed a long time ago in the 1960-ties [1–3]. However, the first experimental signatures of hydrodynamic transport were observed only three decades later in the late 1990-ties in a two-dimensional (2D) electron gas of high-mobility (Al, Ga)As heterostructures [4, 5]. In particular, it was shown that the resistivity decreases with temperature [4, 5], which is known as the Gurzhi effect [1]; see Ref. [6] for the Gurzhi effect in systems with relativisticlike dispersion relation. Later, the characteristic dependence of the resistivity on the channel size was observed in ultra-pure 2D metal palladium cobaltate (PdCoO_2) [7], which agrees with the dependence expected for the Poiseuille flow of the electron fluid.

The realization of the hydrodynamic regime in graphene [8–14] had a strong impact on the development of electron hydrodynamics in solids [15, 16]. As an example of an interesting effect related to a hydrodynamic flow, graphene’s constriction could have higher conduction in the hydrodynamic regime than in the ballistic one [10, 17]. Three-dimensional (3D) Dirac and Weyl semimetals, whose quasiparticles are described by the Dirac and Weyl equations, respectively, could be considered as 3D analogs of graphene [18, 19]. The experimental observation of the dependence of the electric resistivity on the channel width and the violation of the Wiedemann–Franz law with the lowest Lorenz number ever reported indicate the realization of the hydrodynamic transport regime in the Weyl semimetal WP_2 [20]. Recently, a hydrodynamic profile of the static electric current was visualized via stray magnetic fields in a similar Weyl semimetal WTe_2 [21].

In the majority of the experimental and theoretical studies of hydrodynamic transport, the current is driven by a static voltage. A time-dependent or pulsating flow was investigated in Refs. [22, 23]. It was shown that the maximal flow velocity migrates from the centre towards the edges where boundary layers are formed. As an experimentally accessible signature of these layers, a nontrivial dependence of the optical conductivity on the sample size and frequency was proposed.

Motivated by significant attention to the dynamical properties of materials, we study in this paper the response of electron fluid in the hydrodynamic regime in both 3D and 2D samples to a time-dependent drive. We find that a nontrivial double-peak hydrodynamic profile of the electric current appears in the transient regime. These peaks originate from the interplay of the inertial and viscous properties of the electron fluid. We identify the corresponding phase diagram and investigate the effects of the boundary conditions, the channel geometry, and the time-profile of the drive. While the profiles of the electric current are distorted in nozzles and cavities, the double-peak structure remains as long as the fluid sticks to the surfaces of the channel (no-slip boundary conditions) and the driving force changes its sign. We propose to probe the nontrivial current distribution via stray magnetic fields. It is shown that the double-peak current profile leads to a nonmonotonic magnetic field distribution where the in-plane component of the field perpendicular to the flow also acquires peaks near the boundaries. Our estimates suggest that the magnitude

* pavlo.sukhachov@yale.edu

of the magnetic fields is within the reach of modern quantum spin magnetometry (QSM) techniques [24, 25]. While our study confirms and complements the results reported in Ref. [22], we would like to stress that the phase diagram, fluid flows in channels of different geometries, and a nontrivial distribution of the magnetic field were not reported before.

The paper is organized as follows. The model, main equations, and boundary conditions are described in Sec. II. Steady flows are studied by using both analytical and numerical approaches in Sec. III. Section IV is devoted to electron fluid flows driven by an oscillating driving force. Stray magnetic fields generated by hydrodynamic electron currents are considered in Sec. V. The obtained results are summarized in Sec. VI. Through this study, we set $k_B = 1$.

II. MODEL

In this section, we present the key equations, define the boundary conditions, and discuss the model setup.

A. Hydrodynamic equations and model setup

The hydrodynamic equations for the electron fluid include the Navier–Stokes equation, the energy continuity equation, and the electric charge conservation equation. In addition, since the electron fluid is the charged one, one should include Maxwell's equations. Their role, however, is less profound in transport than in, e.g., collective modes [15] or convection [26]. In this work, we consider only slow flows, where the electron fluid velocity \mathbf{u} is much smaller than the Fermi velocity v_F . Therefore, we linearize the hydrodynamic equations and, in the quasistatic approximation, retain only the Gauss law. The Ampere law does not affect hydrodynamic flows in a linearized regime and will be considered only in Sec. V where stray magnetic fields are calculated. The resulting system reads as

$$\frac{w_0}{v_F^2} \partial_t \mathbf{u} - \eta \left(\Delta - \frac{w_0}{v_F^2 \tau \eta} \right) \mathbf{u} - \frac{\eta}{d} \nabla (\nabla \cdot \mathbf{u}) + \nabla P = -en_0 \mathbf{E}, \quad (1)$$

$$\partial_t \epsilon + w_0 (\nabla \cdot \mathbf{u}) = 0, \quad (2)$$

$$-e \partial_t n - en_0 (\nabla \cdot \mathbf{u}) + \sigma \left(-\Delta \varphi + \frac{1}{e} \Delta \mu - \frac{\mu_0}{e T_0} \Delta T \right) = 0, \quad (3)$$

$$(\nabla \cdot \mathbf{E}) = -4\pi e(n - n_0). \quad (4)$$

Here, $w = \epsilon + P$ is the enthalpy, ϵ is the energy density, P is the pressure, n is the electron number density, \mathbf{E} is the electric field, v_F is the Fermi velocity, μ is the chemical potential, T is temperature, τ is the relaxation time describing the relaxation of the total momentum of the fluid [2], φ is the electric potential, and $-e$ is the electron charge. The shear viscosity is denoted as η and we neglect the bulk viscosity, which is small in relativisticlike systems (see, e.g., Ref. [27]). One has the following relation for the shear viscosity $\eta = \eta_{\text{kin}} w_0 / v_F^2$, where $\eta_{\text{kin}} \sim v_F^2 \tau_{\text{ee}}$ is the kinematic shear viscosity and τ_{ee} is the electron-electron scattering time. In graphene, $\eta_{\text{kin}} = v_F^2 \tau_{\text{ee}} / 4$ [28]. For a relativisticlike fluid, $P = \epsilon/d$ and $w = (d+1)\epsilon/d$ where $d = 2, 3$ is the spatial dimension. For our numerical estimates, we use $\tau_{\text{ee}} \approx \hbar/T$ reported for WP₂ [20]. Finally, subscript 0 denotes the global equilibrium values of parameters. The expressions for n_0 and ϵ_0 are given in Appendix A.

The linearized electric and energy currents in the hydrodynamic regime are given by (see, e.g., Ref. [15])

$$\mathbf{J} = -en_0 \mathbf{u} + \sigma \left(\mathbf{E} + \frac{1}{e} \nabla \mu - \frac{\mu_0}{e T_0} \nabla T \right) \quad \text{and} \quad \mathbf{J}^\epsilon = w_0 \mathbf{u}, \quad (5)$$

respectively.

The intrinsic conductivity σ can be estimated in a holographic approach [29–33] and reads as

$$3D: \quad \sigma = \frac{3\pi \hbar v_F^3}{2} (\partial_\mu n) \tau_{\text{ee}}, \quad (6)$$

$$2D: \quad \sigma = \frac{2e^2}{\pi \hbar}. \quad (7)$$

Let us now discuss the model setup. We consider three geometries: (i) straight channel, (ii) nozzle, and (iii) cavity. Nozzle and cavity are schematically shown in Figs. 2(b) and 2(c), respectively. In our numerical calculations, we assume that samples have length L_x along the x -direction and their width is L_y at $x = 0$ and $x = L_x$. The shape of the boundaries is defined analytically by the following expressions:

$$y = \frac{L_N}{2} \left[e^{-(x-L_x/2)^2} - e^{-L_x^2/4} \right] \quad \text{and} \quad y = L_y - \frac{L_N}{2} \left[e^{-(x-L_x/2)^2} - e^{-L_x^2/4} \right], \quad (8)$$

for the nozzle ($L_N > 0$) and cavity ($L_N < 0$) constrictions. Clearly, the width in the middle of long channels ($x = L_x/2$) is $L_y - L_N$. The case of a straight channel corresponds to $L_N = 0$. For simplicity, we assume that all samples are infinite along the z -direction in 3D. The same geometries are considered for 2D materials where the z -direction is omitted.

B. Driving force, boundary conditions, and numerical parameters

An important ingredient needed for the description of hydrodynamic flows in finite samples is boundary conditions. We consider a time-dependent driving force via voltage applied to the side surfaces of the sample

$$\varphi(t, x = 0, y) = 0, \quad \varphi(t, x = L_x, y) = -E_0 f(t) L_x, \quad (9)$$

where E_0 is the magnitude of the electric field and

$$f(t) = \frac{1}{1 + e^{\xi(t_o - t)}} \cos(2\pi\nu t) \quad (10)$$

defines the time dependence of the applied voltage (a wavelet profile of the driving force is considered in Appendix D). Here, ν is the frequency of oscillations, t_o corresponds to the offset time, and ξ defines the steepness of the initial increase. In our analytical analysis, we set $\xi \rightarrow \infty$ and $t_o \rightarrow 0$. The function $f(t)$ is plotted in Fig. 1.

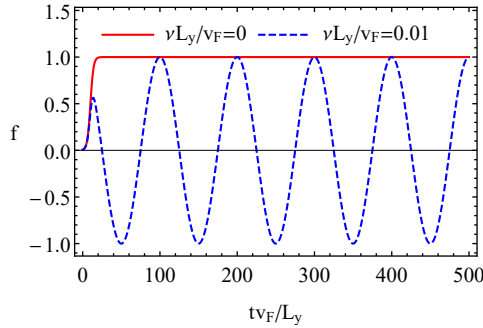


FIG. 1. The dependence of $f(t)$ on time t given by Eq. (10) at $\nu = 0$ (red solid line) and $\nu = 0.01 \times v_F/L_y \approx 22$ MHz (blue dashed line). Other parameters are defined in Eqs. (17) and (18).

In a general case, temperature at the ends of the channel can be different,

$$T(t, x = 0, y) = T_L, \quad T(t, x = L_x, y) = T_R. \quad (11)$$

As to the electron density, we assume also that it is fixed at the boundaries in 3D samples

$$n(t, x = 0, y) = n_0, \quad n(t, x = L_x, y) = n_0. \quad (12)$$

In the 2D case, we employ the “gradual channel” approximation [34, 35]. In this case, instead of the Gauss law (4), the electric field is directly determined by the electron density in the sample

$$\mathbf{E} = \frac{e}{C} \nabla n, \quad (13)$$

where $C = \varepsilon/(4\pi L_g)$ is the capacitance per unit area, ε is the dielectric constant of the substrate, and L_g is the distance to the gate. Therefore, instead of Eq. (12), one can employ

$$n(t, x = 0, y) = n_0, \quad n(t, x = L_x, y) = n_0 + \frac{C}{e} E_0 f(t) L_x \quad (14)$$

in the 2D case.

As for the fluid velocity, we assume that both normal and tangential components of the fluid velocity vanish at the side surfaces or edges (the latter conditions are known as the “no-slip” boundary conditions [36]; see also Refs. [23, 37] for detailed discussion)

$$(\hat{\mathbf{n}} \cdot \mathbf{u}) \Big|_{\{x,y\} \in \mathcal{S}} = 0 \quad \text{and} \quad [\hat{\mathbf{n}} \times \mathbf{u}] \Big|_{\{x,y\} \in \mathcal{S}} = \mathbf{0}, \quad (15)$$

where $\hat{\mathbf{n}}$ is the surface normal and \mathcal{S} is the side surface. The case of more general boundary conditions is briefly addressed in Appendix C. Finally, the electric current should not flow through the sides of the channel, i.e.,

$$(\hat{\mathbf{n}} \cdot \mathbf{J}) \Big|_{\{x,y\} \in \mathcal{S}} = 0. \quad (16)$$

Equations (1) through (5) together with the boundary conditions (9), (11), (12) or (14), (15), and (16) comprise a system of equations that describes the hydrodynamic flow of a charged fluid in a channel.

In our numerical calculations of 3D hydrodynamic flows, we use material parameters for WP₂ [38] and the following typical values of sample sizes and external fields:

$$v_F = 1.4 \times 10^7 \text{ cm/s}, \quad \tau = 0.3 \text{ ns}, \quad T_0 = 10 \text{ K}, \quad \mu_0 = 20 \text{ meV}, \quad E_0 = 2 \text{ mV/m}, \quad (17)$$

$$L_y = 10 \text{ } \mu\text{m}, \quad L_x = 5 \times L_y, \quad \xi = 0.2 \times v_F/L_y \approx 7 \text{ ns}^{-1}, \quad t_o = 10 \times L_y/v_F \approx 0.71 \text{ ns}. \quad (18)$$

In the 2D case, we use the parameters of graphene with $v_F = 1.1 \times 10^8 \text{ cm/s}$, $\mu_0 = 100 \text{ meV}$, $T_0 = 100 \text{ K}$, $\tau \approx 0.1 \text{ ns}$, and $L_g = 100 \text{ nm}$. As for the value of dielectric constant of the substrate, we assume $\varepsilon \approx 3.3$ as in hexagonal boron nitride.

As we show for a steady flow in Sec. III, temperature gradient could play a role similar to the electric field in driving the electron fluid flow. The effect of temperature gradient is, however, weak and leads to a small asymmetry of the electron fluid velocity with respect to $E_0 \rightarrow -E_0$. Therefore, to simplify the presentation, we take into account temperature gradient only in general expressions in Sec. III.

The case of a straight channel, which is infinite along the x -direction, can be easily analyzed analytically. This is done in Secs. III and IV A for steady and time-dependent flows, respectively. In general, nozzle and cavity geometries admit only numerical solutions. The corresponding solutions are presented in Secs. III and IV B for steady and dynamic flows, respectively.

III. STEADY FLOW

As a warm-up, let us begin our analysis with steady flows for a static voltage, i.e., we set $\nu = 0$ in Eq. (10). The results obtained in this section allow us to better understand the role of the time-dependent driving force considered in Sec. IV for nonstationary viscous electron flows.

We start with the case of a steady flow in a channel infinite in the x -direction. In this case, if the ends of the channel are kept at different temperatures, then temperature gradient develops. The corresponding equation can be obtained by calculating the divergence of Eq. (1) and using Eq. (3). Notice that, in view of Eq. (2), the electron fluid is incompressible. Then, after straightforward manipulations, we obtain

$$\Delta T = 0. \quad (19)$$

The solution of this equation with the boundary conditions in Eq. (11) is simple

$$T(t, x, y) = T_L + \frac{T_R - T_L}{L_x} x \quad (20)$$

and corresponds to a constant temperature gradient $\partial_x T(t, x, y) = (T_R - T_L)/L_x$ along the x -direction.

In infinite channels, the electric charge deviations are suppressed due to the Gauss law, $n \approx 0$. Therefore, in the linearized regime with $n = (\partial_\mu n)\mu + (\partial_T n)T$, we obtain $\mu \approx -T(\partial_T n)/(\partial_\mu n)$. Then, the following solution for the x component of the fluid velocity follows from the x -component of Eq. (1):

$$u_x(t, y) = -\frac{\tau v_F^2 n_0}{w_0} \left\{ eE_0 + \frac{1}{n_0} \left[s_0 - n_0 \frac{(\partial_T n)}{(\partial_\mu n)} \right] (\partial_x T) \right\} \left[1 - \frac{\cosh \left(\frac{L_y - 2y}{2\lambda_G} \right)}{\cosh \left(\frac{L_y}{2\lambda_G} \right)} \right], \quad (21)$$

where

$$\lambda_G = \sqrt{\frac{\tau \eta v_F^2}{w_0}} \quad (22)$$

is the Gurzhi length. The terms in the curly brackets of Eq. (21) describe a driving force and the fluid velocity profile is defined by the terms in the square brackets. As one can see, the Poiseuille (parabolic-like) profile of the electric

current is reproduced at $\lambda_G/L_y \gtrsim 1$. In the opposite limit $\lambda_G/L_y \ll 1$, the Ohmic profile with almost uniform velocity is realized.

Next, we provide the numerical results and discuss their key features for the model defined in Sec. II. We focus on the hallmark hydrodynamic characteristics of fluids, i.e., the electron fluid velocity \mathbf{u} . Its nontrivial profile is directly reflected in the electric current density. We present the results for \mathbf{u} in Fig. 2. The velocity in the middle of the channel ($x = L_x/2$) shows the expected Poiseuille profile, which agrees with the analytical results in Eq. (21). The fluid velocity becomes nonuniform along the axis of nozzles and cavities: it increases in nozzles and decreases in cavities. Therefore, transport regimes with different flow velocities could be accessed by carefully engineering the sample.

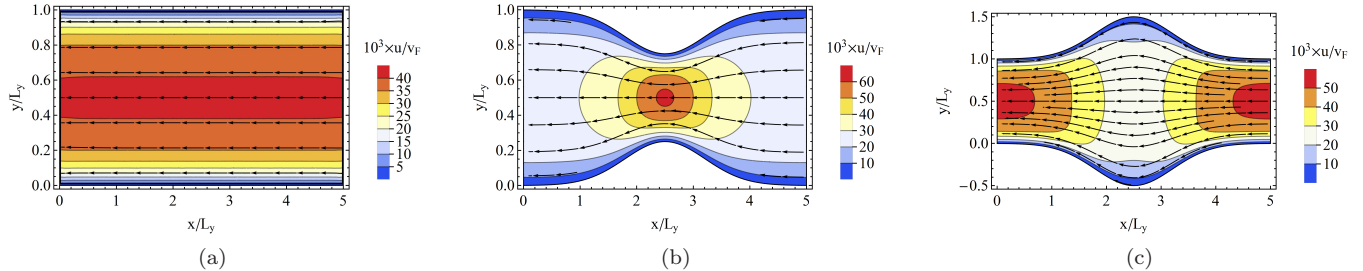


FIG. 2. The profile of fluid velocity $\mathbf{u}(x, y)$ in the straight channel (panel (a)), nozzle (panel (b)), and cavity (panel (c)) geometries. Numerical parameters defined in Sec. II B are used.

IV. TIME-DEPENDENT FLOW

Let us proceed to the case of a time-dependent flow driven by an oscillating voltage; see Eq. (9) for the corresponding boundary conditions.

A. Analytical model

We start with an analytically solvable model of a straight channel infinite along the x -direction. For the sake of simplicity, we assume that the charge and energy densities remain constant, $n = n_0$ and $\epsilon = \epsilon_0$. [The former condition is not needed in 2D where the gradual channel approximation is used.] These approximations are due to strong screening and weak heating effects, respectively. Then the system of equations (1) through (4) reduces to

$$\partial_t u_y - \frac{\eta v_F^2}{w_0} \Delta u_y + \frac{u_y}{\tau} = 0, \quad (23)$$

$$\partial_t u_x - \frac{\eta v_F^2}{w_0} \Delta u_x + \frac{u_x}{\tau} = -\frac{ev_F^2 n_0 E_0}{w_0} f(t, y). \quad (24)$$

We use the no-slip boundary conditions for $u_x(t, x, y)$ and $u_y(t, x, y)$ together with the initial conditions $u_y(t = 0, x, y) = u_x(t = 0, x, y) = 0$. In the 2D case and for the gradual channel approximation, the pressure gradient should be taken into account. Then, the driving force $E_0 f(t, y)$ on the right-hand side of Eq. (24) reads as $E_0 f(t, y) \{1 - 2C / [e^2 (\partial_\mu n)]\}$. This modification does not lead to any qualitative or, for the parameters at hand, even quantitative changes.

The solution to Eq. (23) is trivial, i.e., $u_y(t, x, y) = 0$. Because there is no dependence on the x -coordinate in the model at hand, the solution for $u_x(t, y)$ reads as

$$u_x(t, y) = -\frac{ev_F^2 n_0 E_0}{w_0} \int_0^\infty dt' \int_0^{L_y} dy' G(t - t'; y, y') f(t', y'), \quad (25)$$

where

$$G(t - t'; y, y') = \frac{2}{L_y} \sum_{k=1}^{\infty} e^{-C_k(t-t')/\tau} \theta(t - t') \sin\left(\frac{\pi k y'}{L_y}\right) \sin\left(\frac{\pi k y}{L_y}\right) \quad (26)$$

is the Green function and $C_k = 1 + (\lambda_G \pi k / L_y)^2$. Calculating the integrals over t' and y' in Eq. (25), the solution for the fluid velocity reads as

$$\begin{aligned} u_x(t, y) &= -\frac{ev_F^2 n_0 E_0 \tau}{w_0} \sum_{k=1,3,5,\dots} \frac{4}{\pi k} \sin\left(\frac{\pi k y}{L_y}\right) \frac{2\pi\nu\tau \sin(2\pi\nu t) + C_k [\cos(2\pi\nu t) - e^{-C_k t/\tau}]}{(2\pi\nu\tau)^2 + C_k^2} \\ &\stackrel{t \gg \tau}{\approx} -\frac{ev_F^2 n_0 E_0 \tau}{w_0} \sum_{k=1,3,5,\dots} \frac{4}{\pi k} \sin\left(\frac{\pi k y}{L_y}\right) \frac{2\pi\nu\tau \sin(2\pi\nu t) + C_k \cos(2\pi\nu t)}{(2\pi\nu\tau)^2 + C_k^2}. \end{aligned} \quad (27)$$

As one can already see from the above equation, the spatial dependence of the fluid velocity $u_x(t, y)$ could be rather nontrivial for a nonzero frequency of the driving force. This is related to the interplay of the viscous and dissipative effects on the one hand and the acceleration due to the time-dependent external force on the other hand.

We present the fluid velocity profiles in the transition regime in Fig. 3 for a few values of t . First, we notice that there is a phase shift between the driving force and the fluid velocity due to the acceleration term $\partial_t u_x$ [see also the term $2\pi\nu\tau \sin(2\pi\nu t)$ in Eq. (27)]. Indeed, while the driving force, according to Eq. (10), vanishes at $\nu t \approx (2l+1)/4$ with $l = 0, 1, 2, 3, \dots$, the velocity in a clean system (large $\nu\tau$) passes through zero for $\nu t \approx l/2$; see also Appendix B where the time dependence of the fluid velocity is considered.

Another key feature of the obtained results is the appearance of a *double-peak* structure in the transition regime. First, backflows occur near the boundaries. After delay determined by $\nu\tau$ and λ_G/L_y , the velocity in the bulk also changes sign. The obtained results agree with those in Ref. [22] where a different representation for the solution was used; see also Appendix C.

The reasons for the formation of the double-peak structure could be clearly seen from Eq. (27). Indeed, the first term in the sum, i.e., at $k = 1$, is responsible for the Poiseuille fluid profile where $u_x(t, y)$ vanishes only at the boundaries. The second nonvanishing term has two zeroes inside the sample as a function of y that explains the formation of two peaks if other summands can be neglected. The latter is indeed the case in the viscous regime where $\lambda_G/L_y \gtrsim 1/\pi$. In this regime, the terms with C_k allow for a quick convergence of the sum in Eq. (27) where only the first two terms are relevant. In the opposite limit $\lambda_G/L_y \lesssim 1/\pi$, C_k is large and the sum converges slowly leading to a flat Ohmic-like profile. Finally, comparing the solid and dashed lines in Fig. 3(b), one can see that the velocity profile is well reproduced by taking into account only the first two nonvanishing terms in the sum in Eq. (27).

For a nonzero $\nu\tau$, the convergence of the sum depends on t . Indeed, while at $\nu t \approx l/2$ the summand is $\propto 1/k^3$, for $\nu t \approx (2l+1)/4$, it decays as $\propto 1/k^5$. This explains why the fluid velocity profile changes its form with time.

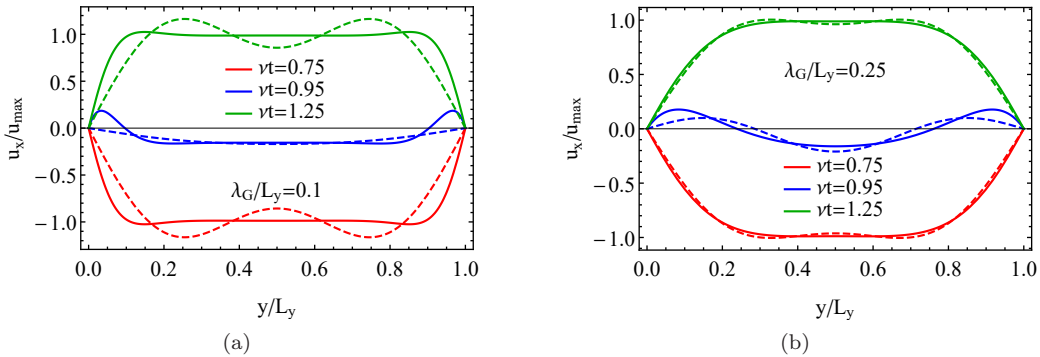


FIG. 3. The fluid velocity profiles for a few values of νt at $\lambda_G = 0.1 \times L_y$ (panel (a)) and $\lambda_G = 0.25 \times L_y$ (panel (b)). Solid and dashed lines correspond to 500 and 2 summands in Eq. (27), respectively.

Let us clarify the physics behind the nontrivial dynamics of the fluid velocity. There are two dimensionless parameters that determine the profile of the flow: (i) $\nu\tau$ and (ii) λ_G/L_y . The first parameter quantifies the inertial properties of the fluid and the second parameter is related to its viscosity. We present the phase diagram of the system in the plane of these parameters in Fig. 4 by using the curvature of the fluid flow (see Appendix B for its definition) and the phase shift between the fluid velocity and the driving force as guides. We identify three main regimes. The first regime is the Ohmic one where the current profile is flat in the middle of the channel. It occurs for small $\nu\tau \ll 1$ and $\lambda_G/L_y \ll 1$. If the frequency is large enough and the viscosity is small but nonnegligible, the double peaks might occur near boundaries. However, they are hardly discernible on top of abrupt changes in the fluid profile. The second regime is the viscous regime of the fluid flow. It requires large viscosity $\lambda_G/L_y \gtrsim 1$ and can be easily identified via the curvature of the velocity profile; see Fig. 4(a). Finally, the third regime has a noticeable phase shift between the driving force and the fluid velocity; see Fig. 4(b). For large $\nu\tau$, the driving force and the fluid velocity can oscillate

in antiphase, i.e., the shift reaches $\pi/2$. This regime is characterized by a double-peak profile of the fluid velocity. While the main requirement for the realization of the peaks is $\nu\tau \gtrsim 1$, they are well manifested if the fluid velocity has a well-pronounced Poiseuille profile, i.e., λ_G/L_y should be nonnegligible.

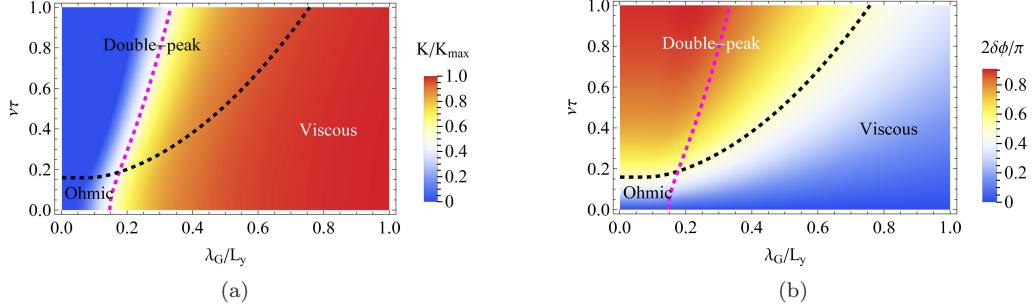


FIG. 4. The phase diagram of the system in the plane of $\nu\tau$ and λ_G/L_y . We show the curvature of the fluid flow in the middle of the channel in panel (a) and the phase difference $\delta\phi$ between the fluid velocity and the driving force in panel (b). The curvature of the fluid profile K is defined in Appendix B. Black and magenta dashed lines correspond to $\delta\phi = \pi/4$ and $K = K_{\max}/2$, respectively.

Finally, let us comment on the role of the boundary conditions and the time dependence of the driving force. As we show in Appendix C, the boundary conditions for the fluid velocity play an important role in the formation of double peaks. In particular, there are no peaks for the free-surface boundary conditions where the fluid velocity profile remains flat. Still, due to the dominant role of the inertial term $\sim \nu\tau$, the oscillations of the velocity and the driving force are shifted in phase. As for the time-profile of the driving force, the formation of the double-peak structure does not rely on the specific harmonic form used in Eq. (27) and should occur as long as the driving force changes its sign. This is confirmed by the results for a wavelet profile of the driving force given in Appendix C.

B. Numerical results

In this section, to support our analytical findings in Sec. IV A, we present numerical results for dynamical electron fluid flow in the straight channel, nozzle, and cavity geometries. We demonstrate that while the details of the velocity distribution noticeably depend on the geometry of the channel, the double-peak profile of the fluid velocity remains in the transient regime and qualitatively agrees with the analytical results in Sec. IV A.

We focus on the most interesting case of the transition regime where the driving force changes its sign. It occurs at $\nu t \approx (2l + 1)/4$ with $l = 0, 1, 2, 3, \dots$. As one can see from Fig. 5, after a short delay determined by $\nu\tau$, the fluid velocity also starts to change its sign. The transition, is, however, rather nontrivial. First, backflows occur near the boundaries leading to a *double-peak* structure (see the blue dashed lines in Fig. 5). Then, the velocity in the bulk also changes sign (see the green dotted lines in Fig. 5). Finally, the velocity profile deforms and the peaks flatten ultimately leading to a reversed profile compared to that shown by the red lines in Fig. 5. These results perfectly agree with our analytical considerations in Sec. IV A.

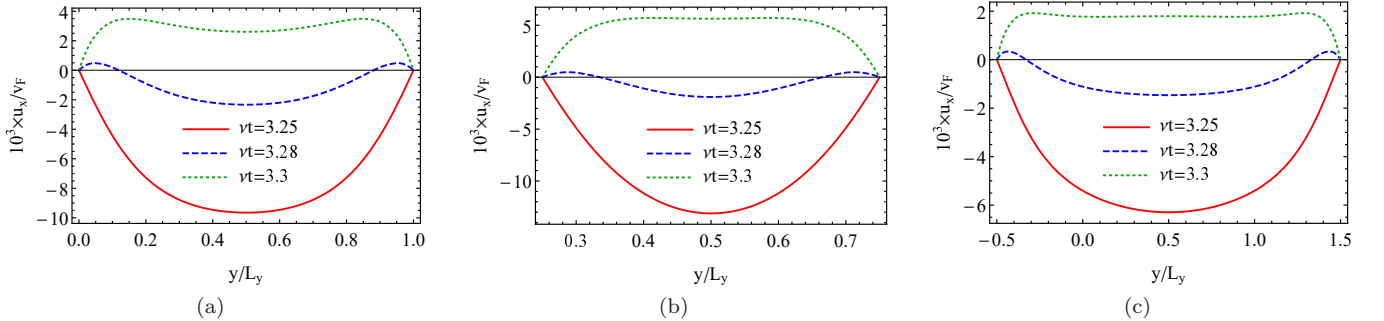


FIG. 5. The fluid velocity $u_x(t, x, y)$ at $x = L_x/2$ for $\nu t = 3.25$ (red solid line), $\nu t = 3.28$ (blue dashed line), and $\nu t = 3.3$ (green dotted line). Other parameters are defined in Sec. II B. We use the channel (panel (a)), nozzle (panel (b)), and cavity geometries (panel (c)).

The fluid flow in nozzle and cavity is visualized in Figs. 6 and 7, respectively. A double-peak profile of the velocity is clearly seen in Figs. 6(b) and 7(b); see also Figs. 5(b) and 5(c) for the velocity profile at $x = L_x/2$. Therefore, the formation of the double peaks in the transient regime is robust with respect to the channel geometry.

The overall distribution of the velocity is, as expected, modified. As in the case of the steady flow, the velocity increases in nozzle and diminishes in cavity. This could be used to effectively modulate the flow velocity and access different transport regimes in the same sample. For example, by driving a large current through the sample it might be even possible to observe a transition from sub- to supersonic flow in nozzles [39].

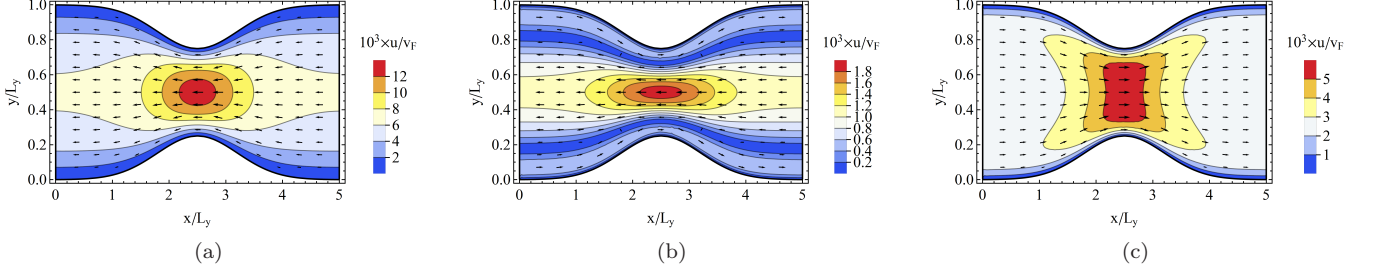


FIG. 6. The distribution of the fluid velocity $\mathbf{u}(t, x, y)$ in the nozzle geometry at $\nu t = 3.25$ (panel (a)), $\nu t = 3.28$ (panel (b)), and $\nu t = 3.3$ (panel (c)). Other parameters are defined in Sec. II B.

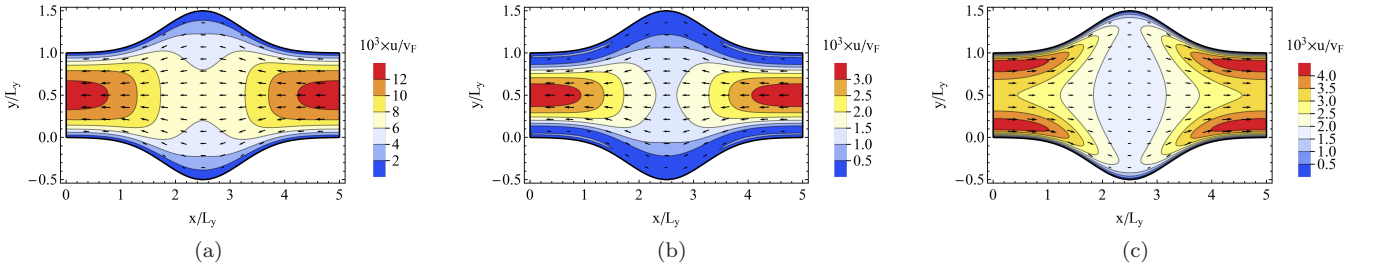


FIG. 7. The distribution of the fluid velocity $\mathbf{u}(t, x, y)$ in the cavity geometry at $\nu t = 3.25$ (panel (a)), $\nu t = 3.28$ (panel (b)), and $\nu t = 3.3$ (panel (c)). Other parameters are defined in Sec. II B.

V. STRAY MAGNETIC FIELD

In this section, motivated by the recent studies of viscous flow via the QSM in Refs. [13, 21], we present the results for stray magnetic fields generated by the electric current in the channel. In order to find the corresponding magnetic field, we employ the standard Maxwell equations in the quasistatic approximation

$$\nabla \times \mathbf{B}(t, \mathbf{r}) = \frac{4\pi}{c} \mathbf{j}(t, \mathbf{r}) + \frac{1}{c} \partial_t \mathbf{E}(t, \mathbf{r}) \quad \text{and} \quad \nabla \cdot \mathbf{B}(t, \mathbf{r}) = 0. \quad (28)$$

This approximation is valid for sufficiently small frequencies (e.g., $\nu \ll \sigma_0$ with σ_0 being the Ohmic conductivity). By introducing the vector potential $\mathbf{A}(t, \mathbf{r})$ and using the Coulomb gauge $\nabla \cdot \mathbf{A}(t, \mathbf{r}) = 0$, we obtain

$$\Delta \mathbf{A}(t, \mathbf{r}) = \frac{4\pi}{c} \mathbf{J}(t, \mathbf{r}). \quad (29)$$

Since the current realizations of the QSM are most suitable for 2D or quasi-2D materials, we consider a long graphene ribbon where the width L_y is much smaller than the length of the ribbon. The ribbon is located in the $x-y$ plane at $z = 0$ and the gate is at $z = -L_g$. If the magnetic permeability of the gate is small, both vector potential and its derivatives are continuous at gate's surfaces [40]. In addition, the vector potential should diminish for large z , i.e., $\mathbf{A}(t, \mathbf{r}_\perp, z \rightarrow \pm\infty) \rightarrow 0$. Then, by using the fact that the current is localized in the film, $\mathbf{J}(t, \mathbf{r}) = \mathbf{J}(t, \mathbf{r}_\perp) \delta(z)$, and performing the Fourier transform in the in-plane coordinates, we obtain

$$\mathbf{A}(t, \mathbf{q}, z) = -\frac{2\pi}{cq} \mathbf{J}(t, \mathbf{q}) e^{-q|z|}, \quad (30)$$

where

$$\mathbf{J}(t, \mathbf{q}) = \int d^2 \mathbf{r}_\perp e^{-i\mathbf{q} \cdot \mathbf{r}_\perp} \mathbf{J}(t, \mathbf{r}_\perp). \quad (31)$$

We find that the components of the magnetic field in the coordinate space are

$$B_x(t, \mathbf{r}_\perp, z) = -\frac{2\pi}{c} \int \frac{d^2 \mathbf{q}}{(2\pi)^2} e^{i\mathbf{q} \cdot \mathbf{r}_\perp} J_y(t, \mathbf{q}) \operatorname{sgn}(z) e^{-q|z|}, \quad (32)$$

$$B_y(t, \mathbf{r}_\perp, z) = \frac{2\pi}{c} \int \frac{d^2 \mathbf{q}}{(2\pi)^2} e^{i\mathbf{q} \cdot \mathbf{r}_\perp} J_x(t, \mathbf{q}) \operatorname{sgn}(z) e^{-q|z|}, \quad (33)$$

$$B_z(t, \mathbf{r}_\perp, z) = -i \frac{2\pi}{c} \int \frac{d^2 \mathbf{q}}{(2\pi)^2} e^{i\mathbf{q} \cdot \mathbf{r}_\perp} \frac{[\mathbf{q} \times \mathbf{J}(t, \mathbf{q})]_z}{q} e^{-q|z|}. \quad (34)$$

In the case of a long straight ribbon, $J_y(t, \mathbf{r}_\perp) = 0$, and there is no dependence on the x -coordinate. Therefore, the only nontrivial components of the magnetic field are $B_y(t, y, z)$ and $B_z(t, y, z)$ given in Eqs. (33) and (34). In addition, since $\mathbf{J}(t, \mathbf{q}) = 2\pi\delta(q_x)\mathbf{J}(t, q_y)$, the integral over q_x can be trivially taken.

In what follows, we present the result for the magnetic field for three different profiles of the electric current: (i) Ohmic with $J_x(t, y) = e^2 v_F^2 n_0^2 \tau E_0 / w_0$, (ii) Poiseuille $J_x(t, y) = -en_0 u_x(t, y)$ with $u_x(t, y)$ defined in Eq. (21) at $\partial_x T = 0$, and (iii) double-peak, where velocity is given in Eq. (27). We use $\nu t = 3$, $\nu\tau = 1$, and $\lambda_G/L_g = 0.1$ for the double-peak profile in Eq. (27). In the case of the Poiseuille profile, we set $\nu \rightarrow 0$. The electric current profiles are presented in Fig. 8. Notice that since the double-peak profile is realized in the transient regime, its magnitude is smaller than that for a steady flow.

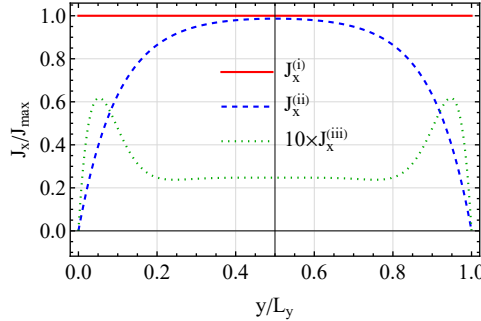


FIG. 8. The normalized electric current profiles used for calculating the magnetic field distribution. Red solid line corresponds to the Ohmic profile $J_x^{(i)}$, blue dashed line describes the Poiseuille profile $J_x^{(ii)}$, and the green dotted line shows the double-peak profile $J_x^{(iii)}$. We use $\nu t = 3$, $\nu\tau = 1$, and $\lambda_G/L_g = 0.1$ in Eq. (27) for the double-peak profile and set $\nu \rightarrow 0$ for the Poiseuille one.

By using the typical numerical parameters for graphene [see Sec. II B], we estimate the following characteristic value of the magnetic field:

$$B_{\text{char}} = \frac{e^2 v_F^2 n_0^2 \tau E_0}{c w_0} \approx 0.12 E_0 \left[\frac{\text{V}}{\text{cm}} \right] \text{ G}, \quad (35)$$

which is essentially the Ohmic current density divided by the speed of light. As we will show below, the typical values of generated magnetic fields are of the order of B_{char} . For example, the total current $I \approx 1 \mu\text{A}$ considered in Ref. [13] is equivalent to $E_0 \sim 10^{-3} \text{ V/cm}$ and $B_{\text{char}} \sim 10^{-2} \mu\text{T}$ for the parameters used in our study. The magnitude of such oscillating magnetic fields is within the range of the QSM [25, 41]. However, it could be experimentally challenging to probe these fields in view of their relatively high frequency. While the full time-evolution of the current could not be traced during a single period, the periodicity of the drive gives a chance to observe nontrivial field distribution.

The obtained magnetic field profiles at fixed $z = 0.1 \times L_y$ are shown in Fig. 9. The magnetic field for a double-peak current profile at a few values of z is presented in Fig. 10. The y -component of the field attains its maximal value in the middle of the ribbon and gradually diminishes away from it. The z -component changes its sign across the ribbon and its absolute value has maxima near the edges of the sample. As one can see, the field distribution for Ohmic and Poiseuille profiles are qualitatively similar albeit have a slightly different curvature at $y = L_y/2$. Nevertheless, this subtle difference corresponds to qualitatively different electric current profiles.

The distribution of the magnetic field for the double-peak profile of the current is different from both Ohmic and Poiseuille currents. Among the most noticeable features, we notice a double-peak structure in B_y with two symmetric peaks near the edges; see Figs. 9(a) and 10. In addition, the peaks in the z -component of the field are steeper and might be even supplemented with additional extrema for $z \ll L_y$. These features could be used to pinpoint the double-peak profile of the electric current. It is worth noting, however, that since the double-peak structure appears in a transition regime, the magnitude of the electric current and, consequently, the generated magnetic field is small compared to that for the steady state currents; see Fig. 9 where we multiplied the results by 10 for a time-dependent drive.

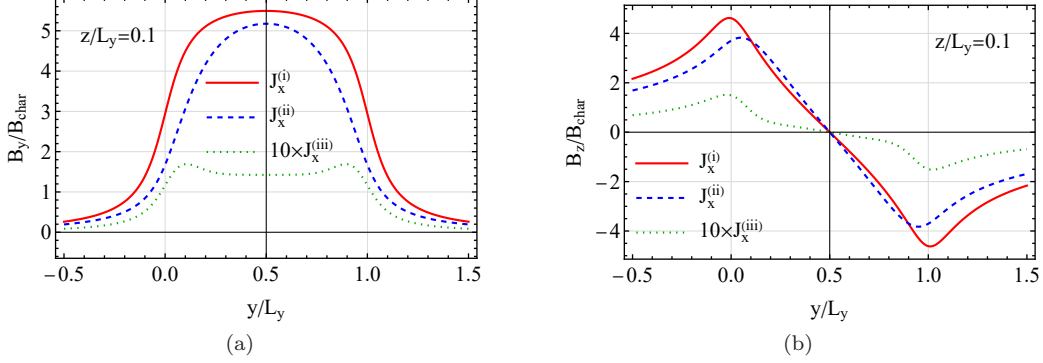


FIG. 9. The normalized magnetic field profiles defined in Eqs. (33) and (34) at $z/L_y = 0.1$. Red solid, blue dashed, and green dotted lines correspond to Ohmic $J_x^{(i)}$, Poiseuille $J_x^{(ii)}$, and double-peak $J_x^{(iii)}$ profiles of the electric current. We normalized the results by the characteristic value of the magnetic field defined in Eq. (35).

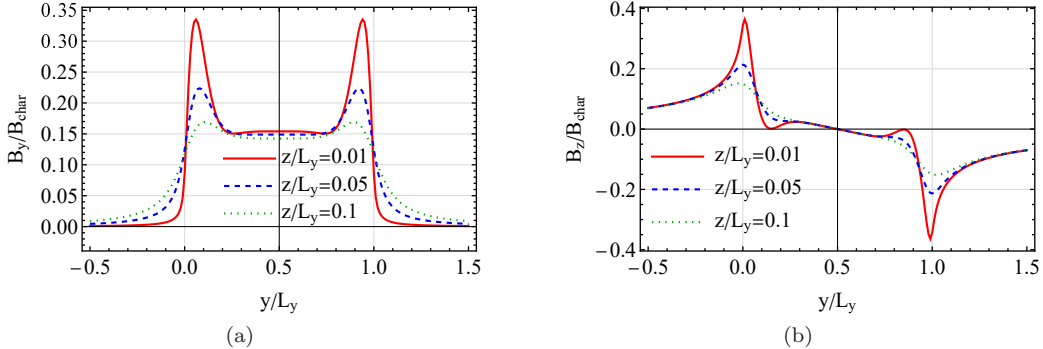


FIG. 10. The normalized magnetic field profiles defined in Eqs. (33) and (34) for the double-peak profile of the electric current for a few values of z : $z = 0.01 \times L_y$ (red solid line), $z = 0.05 \times L_y$ (blue dashed line), $z = 0.1 \times L_y$ (green dotted line). We normalized the results by the characteristic value of the magnetic field defined in Eq. (35).

Before finalizing this section, let us briefly address the role of the gate in the magnetic field distribution. As we discussed before, the thin gate made of material with small magnetic permeability does not alter the vector potential and, consequently, the magnetic field distribution [42]. If the gate has a large magnetic permeability, the boundary conditions for the vector potential play an important role. In particular, in the limit of infinitely large permeability, the spatial derivative of the vector potential vanishes at the gate, i.e., $\partial_z \mathbf{A}(t, \mathbf{r}_\perp, z = -L_g) = 0$. The generalization of the above calculations is straightforward in this case, therefore, we do not present it here. We checked that while the magnetic field distribution near the gate (at $z < 0$) noticeably changes, it remains qualitatively the same above the sample, i.e., at $z > 0$, where it could be conveniently measured via the QSM. Furthermore, the distortion of the magnetic field could be easily avoided by using gates with low magnetic permeability made from, e.g., graphite, copper, platinum, etc.

VI. SUMMARY

We studied steady and transient flows of the electron liquid in channels (3D) and ribbons (2D) of different shapes including the straight channel/ribbon, nozzle, and cavity geometries. Among the key findings of our work is a nontrivial double-peak hydrodynamic profile for a transient flow that is manifested in a stray magnetic field. While we used a relativisticlike dispersion relation of quasiparticles, the obtained results are general and could be applied to materials with other energy dispersions.

Our findings for a straight wire are in good agreement with those in Ref. [22]. In this work, however, we represented the solution in a different form. This allowed us to identify dimensionless quantities that determine the dynamics of the electron fluid in the transient regime and the corresponding phase diagram; see Sec. IV A and Fig. 4. In essence, the double peaks arise due to the interplay of the inertial and viscous properties where the former lead to a phase difference between the driving force and the hydrodynamic current and the latter allow for a double-peak profile to manifest. Our analytical results agree well with the finite-element numerical calculations. While the velocity distribution is noticeably affected by the geometry of samples, the double-peak profile is robust as long as the fluid sticks to the boundaries (no-slip boundary conditions). As for the time dependence of the driving force, the key requirement is the presence of well-defined transition regions where the force changes its sign.

The double-peak profile of the hydrodynamic current is manifested in a stray magnetic field which could be measured via the quantum spin magnetometry. In the case of a straight ribbon, we found that, similarly to the current density, the in-plane magnetic field component perpendicular to the flow acquires a nontrivial profile with symmetric peaks near the boundaries; see Sec. V. The normal to the ribbon component of the field also shows nonmonotonic behavior with additional extrema compared to the magnetic field for both Ohmic (flat) and Poiseuille (parabolic) profiles of current.

In addition, we demonstrated that nozzles and cavities can be used to locally enhance and reduce velocity of the electron fluid, respectively. In particular, nozzles can be employed to reach high velocities and, potentially, achieve a nonlinear regime. It could be possible even to attain a choked flow regime [43]. Therefore, nozzles and cavities could be important in creating hydrodynamic electronics similar to conventional plumbing.

ACKNOWLEDGMENTS

The Authors acknowledge useful communications with I. A. Shovkovy and P. Surówka. P.O.S. acknowledges the support through the Yale Prize Postdoctoral Fellowship in Condensed Matter Theory.

Appendix A: Thermodynamic relations

In this Appendix, we present a few thermodynamic relations that are used in numerical estimates in the main text. In the case of a linear response, we use the following relations:

$$\nabla n = (\partial_\mu n) \nabla \mu + (\partial_T n) \nabla T, \quad (\text{A1})$$

$$\nabla \epsilon = (\partial_\mu \epsilon) \nabla \mu + (\partial_T \epsilon) \nabla T. \quad (\text{A2})$$

Here, n and ϵ are the electric charge and energy densities, μ is the chemical potential, and T is temperature. We find it convenient for numerical calculations to rewrite the dynamical equations in Sec. II in terms of n and ϵ . By using Eqs. (A1) and (A2), we find

$$\nabla \mu = \frac{(\partial_T \epsilon) \nabla n - (\partial_T n) \nabla \epsilon}{(\partial_\mu n)(\partial_T \epsilon) - (\partial_T n)(\partial_\mu \epsilon)}, \quad (\text{A3})$$

$$\nabla T = \frac{(\partial_\mu n) \nabla \epsilon - (\partial_\mu \epsilon) \nabla n}{(\partial_\mu n)(\partial_T \epsilon) - (\partial_T n)(\partial_\mu \epsilon)}. \quad (\text{A4})$$

Next, let us present the key thermodynamic variables. In a 3D relativisticlike case, the electron number density n and the energy density ϵ read

$$n = N_W \frac{\mu (\mu^2 + \pi^2 T^2)}{6\pi^2 v_F^3 \hbar^3}, \quad (\text{A5})$$

and

$$\epsilon = N_W \frac{1}{8\pi^2 \hbar^3 v_F^3} \left(\mu^4 + 2\pi^2 T^2 \mu^2 + \frac{7\pi^4 T^4}{15} \right), \quad (\text{A6})$$

respectively. Here, N_W is the number of Weyl nodes and v_F is the Fermi velocity. The electron number density n and the energy density ϵ for 2D relativisticlike spectrum are

$$n = -N_g \frac{T^2}{2\pi v_F^2 \hbar^2} \left[\text{Li}_2 \left(-e^{\mu/T} \right) - \text{Li}_2 \left(-e^{-\mu/T} \right) \right] \quad (\text{A7})$$

and

$$\epsilon = -N_g \frac{T^3}{\pi v_F^2 \hbar^2} \left[\text{Li}_3 \left(-e^{\mu/T} \right) + \text{Li}_3 \left(-e^{-\mu/T} \right) \right], \quad (\text{A8})$$

respectively. Here, $N_g = 4$ accounts for the valley and spin degeneracy in graphene.

Appendix B: Fluid flow velocity

In this Appendix, we present the results for the normalized flow velocity at a few values of dimensionless frequency of the driving force $\nu\tau$, where τ is the momentum relaxation time, and the dimensionless Gurzhi length λ_G/L_y where L_y is the width of the channel [see Eq. (22) for the definition of the Gurzhi length]. The velocity profile is defined in Eq. (27). As one can see from Figs. 11 and 12, due to the combined effect of the oscillating driving force and the no-slip boundary conditions, the velocity profiles become distorted for large $\nu\tau \gtrsim 1$. If one takes a cut at fixed $\nu\tau$, this would correspond to the double-peak profile in $u_x(t, y)$ shown in Fig. 3. Another important ingredient that allows for the presence of the peaks is the viscosity quantified by the Gurzhi length. At small viscosity $\lambda_G/L_y \lesssim 1$, the fluid velocity profile is flat and rapidly changes only near boundaries. In this case, the peaks are hardly distinguishable; see Fig. 12(a). On the other hand, the double-peak features are suppressed for large values of λ_G/L_y because the viscosity reduces the phase shift between the driving force and the fluid velocity. Thus, as we discussed in the main text [see Fig. 4], the double-peak profile of the hydrodynamic velocity requires large $\nu\tau$ and intermediate values of viscosity (or, equivalently, λ_G).

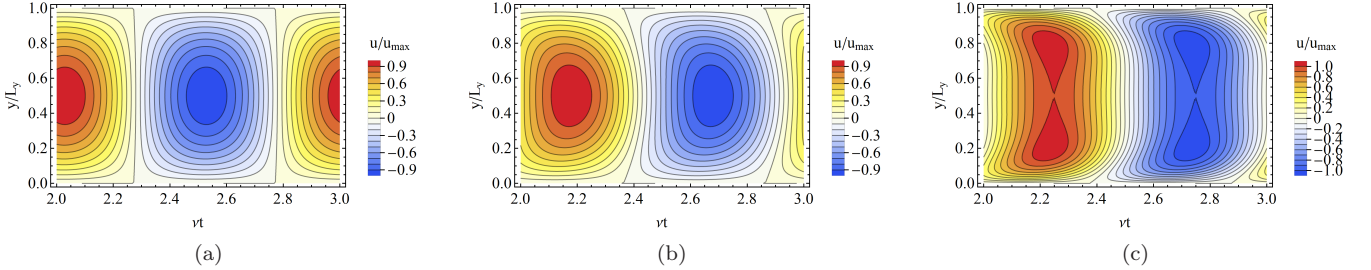


FIG. 11. The normalized fluid velocity $\mathbf{u}(t, x, y)$ defined in Eq. (27) for $\nu\tau = 0.1$ (panel (a)), $\nu\tau = 1$ (panel (b)), and $\nu\tau = 10$ (panel (c)). In all panels, we fixed $\lambda_G/L_y = 0.5$.

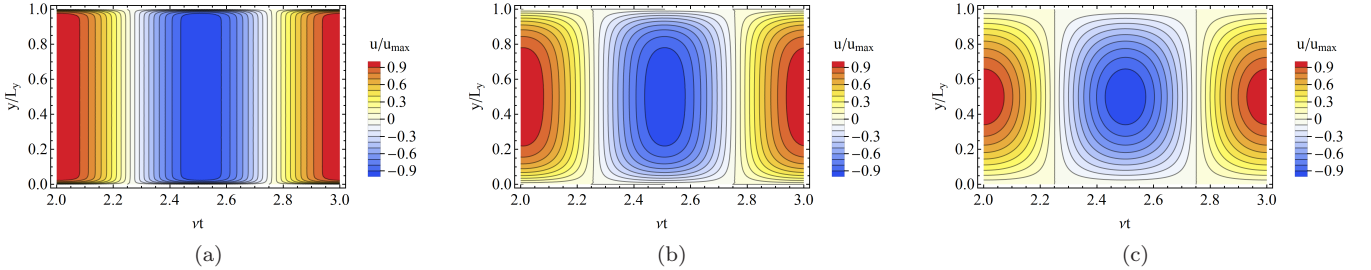


FIG. 12. The normalized fluid velocity $\mathbf{u}(t, x, y)$ defined in Eq. (27) for $\lambda_G/L_y = 0.01$ (panel (a)), $\lambda_G/L_y = 0.1$ (panel (b)), and $\lambda_G/L_y = 1$ (panel (c)). In all panels, we fixed $\nu\tau = 0.01$.

Finally, let us define the curvature of the fluid velocity profile which was used in Sec. IV A. We fit the velocity profile at the time when the velocity reaches its maximum via the parabolic function $a_1 + a_2(y/L_y)^2$. Then, the curvature K is defined as $K = -a_2/a_1$. In addition, to avoid the effects of the boundaries, we used only the part of the profile with $0.25 \leq y/L_y \leq 0.75$. The curvature is maximal for the hydrodynamic profile of the current and vanishes for the Ohmic one.

Appendix C: Role of boundary conditions

In the Appendix, we briefly investigate the role of the boundary conditions in the formation of the double-peak structure discussed in Sec. IV. In general, the boundary conditions are neither no-slip nor free-surface. By using the straight infinite along the x -direction channel as an example, we define

$$u_x(t, y = 0) + l_{s,1} \partial_y u_x(t, y = 0) = 0 \quad \text{and} \quad u_x(t, y = L_y) + l_{s,2} \partial_y u_x(t, y = L_y) = 0. \quad (\text{C1})$$

Here, $l_{s,1}$ and $l_{s,2}$ are the slip lengths, which could be different at different surfaces. No-slip boundary conditions correspond to $l_s \rightarrow 0$ and the free-surface ones are realized for $l_s \rightarrow \infty$. For illustrative purposes, we consider three types of the boundary conditions:

$$\text{no-slip: } u_x(t, y = 0) = 0, \quad u_x(t, y = L_y) = 0, \quad (\text{C2})$$

$$\text{free-surface: } \partial_y u_x(t, y = 0) = 0, \quad \partial_y u_x(t, y = L_y) = 0, \quad (\text{C3})$$

$$\text{mixed: } u_x(t, y = 0) = 0, \quad \partial_y u_x(t, y = L_y) = 0. \quad (\text{C4})$$

The fluid velocity can be found along the same lines as in Sec. IV A. By following Ref. [22], we use a different representation for the solution. As one can see from Eq. (27), the time dependence of $u_x(t, y)$ is given by periodic functions and an exponential term. For $t \gg \tau$, the exponential term can be neglected. Then the Navier-Stokes equation (24) can be solved by replacing $\cos(2\pi\nu t) \rightarrow e^{-2\pi i\nu t}$ in the driving force, solving for $u_x(t, y) = e^{-2\pi i\nu t} u_x(y)$, and taking the real part of the final result. The corresponding time-dependent solutions for the fluid velocity are

$$\text{no-slip: } u_x(t, y) = -\frac{e\tau v_F^2 n_0 E_x}{w_0} \operatorname{Re} \left\{ \frac{e^{-2\pi i\nu t}}{1 - 2\pi i\nu\tau} \left[1 - \frac{\cosh\left(\frac{L_y - 2y}{2\lambda_G}\sqrt{1 - 2\pi i\nu\tau}\right)}{\cosh\left(\frac{L_y}{2\lambda_G}\sqrt{1 - 2\pi i\nu\tau}\right)} \right] \right\}, \quad (\text{C5})$$

$$\text{free-surface: } u_x(t, y) = -\frac{e\tau v_F^2 n_0 E_x}{w_0} \operatorname{Re} \left\{ \frac{e^{-2\pi i\nu t}}{1 - 2\pi i\nu\tau} \right\}, \quad (\text{C6})$$

$$\text{mixed: } u_x(t, y) = -\frac{e\tau v_F^2 n_0 E_x}{w_0} \operatorname{Re} \left\{ \frac{e^{-2\pi i\nu t}}{1 - 2\pi i\nu\tau} \left[1 - \frac{\cosh\left(\frac{L_y - y}{\lambda_G}\sqrt{1 - 2\pi i\nu\tau}\right)}{\cosh\left(\frac{L_y}{\lambda_G}\sqrt{1 - 2\pi i\nu\tau}\right)} \right] \right\}. \quad (\text{C7})$$

We compare the profile of the fluid velocities for the three boundary conditions in Fig. 13. As one can see, no peaks appear for the free-surface boundary conditions. In the case of the mixed boundary conditions, there is only one peak, which appears near the surface with the no-slip boundary condition. Therefore, as with the Poiseuille profile in the steady case, the peaks in the driven regime require the fluid to stick to the surfaces of the channel.

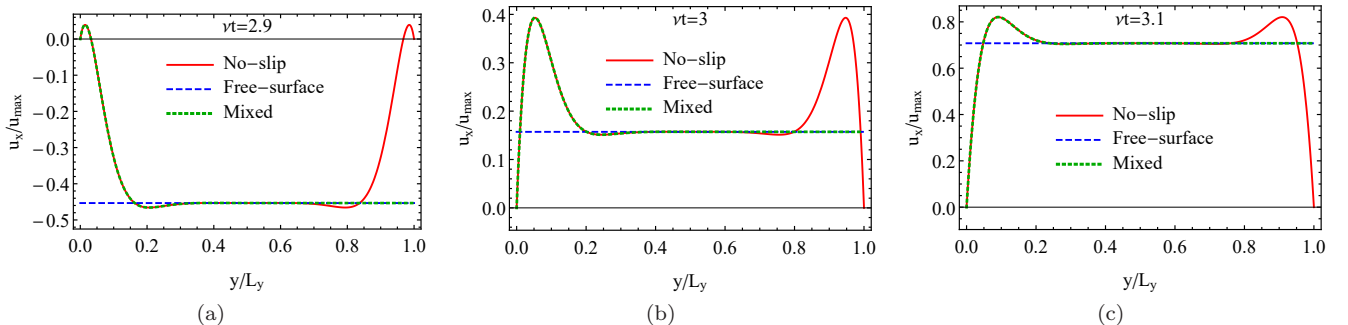


FIG. 13. The normalized fluid velocity $u_x(t, y)$ for $\nu t = 2.9$ (panel (a)), $\nu t = 3$ (panel (b)), and $\nu t = 3.1$ (panel (c)). The boundary conditions are no-slip (red solid lines), free-surface (blue dashed lines), and mixed (green thick dotted lines). In all panels, we fixed $\nu\tau = 1$ and $\lambda_G/L_y = 0.1$. We used Eqs. (C5), (C6), and (C7) for the no-slip, free-surface, and mixed boundary conditions, respectively.

Appendix D: Role of time-profile of driving force

In addition to the boundary conditions and the channel geometry, let us investigate the role of the time-profile of the driving force on the formation of double peaks. For illustrative purposes, we use a wavelet profile defined as

$$f(t) = \frac{1}{1 + e^{\xi(t_o - t)}} \cos(2\pi\nu t) e^{-\xi_1(t - t_{\text{centr}})^2}. \quad (\text{D1})$$

This function is plotted in Fig. 14 for $\nu = 0$ and $\nu = 0.02 \times v_F/L_y$.

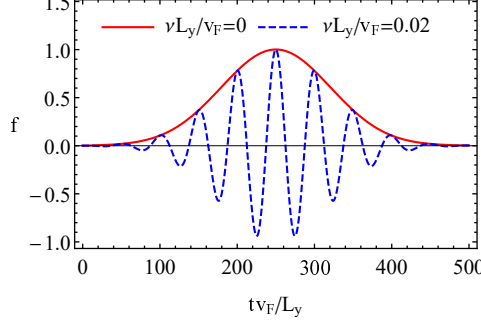


FIG. 14. The dependence of $f(t)$ given by Eq. (10) on time t at $\nu = 0$ (red solid line) and $\nu = 0.02 \times v_F/L_y \approx 44$ MHz (blue dashed line). We set $\xi = 0.2 \times v_F/L_y$, $t_o = 10 \times L_y/v_F$, $t_{\text{centr}} = 250 \times L_y/v_F$, and $\xi_1 = 10^{-4} \times v_F^2/L_y^2$.

The numerical results for the fluid velocity in the straight channel are shown in Fig. 15. As one can see, a double-peak profile also appears for a wavelet in the transition region. Therefore, the driving force should not be necessarily harmonic. The only requirement is the presence of transition regions where the force changes its sign.

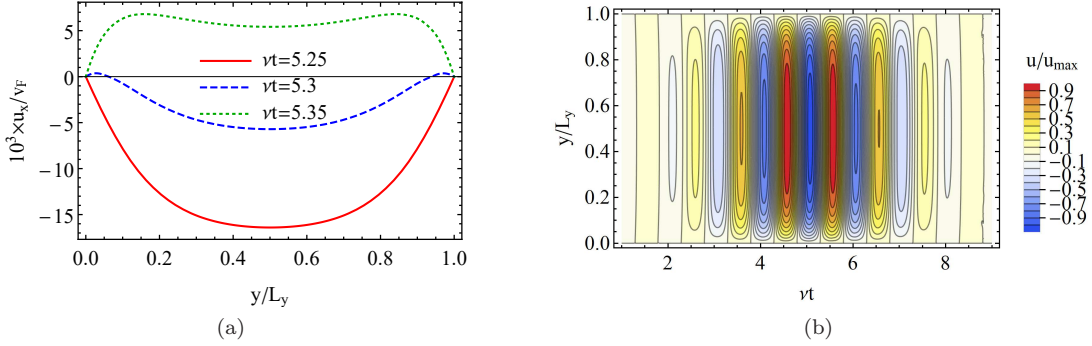


FIG. 15. Panel (a): The fluid velocity $u_x(t, x, y)$ at $x = L_x/2$ for $\nu t = 5.25$ (red solid line), $\nu t = 5.3$ (blue dashed line), and $\nu t = 5.35$ (green dotted line). Panel (b): The fluid velocity $u_x(t, x, y)$ at $x = L_x/2$ for several values of t and y . In all panels, we use the channel geometry and the driving force defined in Eq. (D1).

-
- [1] R. Gurzhi, Minimum of resistance in impurity-free conductors, *JETP* **17**, 521 (1963).
[2] R. N. Gurzhi, Hydrodynamic effects in solids at low temperature, *Sov. Phys. Uspekhi* **11**, 255 (1968).
[3] H. Nielsen and B. I. Shklovskii, Heat transfer and second sound in dielectrics at large drift velocities of the phonon gas, *Zh. Eksp. Teor. Fiz.* **29**, 396 (1969).
[4] L. W. Molenkamp and M. J. de Jong, Observation of Knudsen and Gurzhi transport regimes in a two-dimensional wire, *Solid State Electron.* **37**, 551 (1994).
[5] M. J. De Jong and L. W. Molenkamp, Hydrodynamic electron flow in high-mobility wires, *Phys. Rev. B* **51**, 13389 (1995).
[6] O. Kashuba, B. Trauzettel, and L. W. Molenkamp, Relativistic Gurzhi effect in channels of Dirac materials, *Phys. Rev. B* **97**, 205129 (2018).
[7] P. J. W. Moll, P. Kushwaha, N. Nandi, B. Schmidt, and A. P. Mackenzie, Evidence for hydrodynamic electron flow in PdCoO₂, *Science* **351**, 1061 (2016).

- [8] J. Crossno, J. K. Shi, K. Wang, X. Liu, A. Harzheim, A. Lucas, S. Sachdev, P. Kim, T. Taniguchi, K. Watanabe, T. A. Ohki, and K. C. Fong, Observation of the Dirac fluid and the breakdown of the Wiedemann-Franz law in graphene, *Science* **351**, 1058 (2016).
- [9] F. Ghahari, H.-Y. Xie, T. Taniguchi, K. Watanabe, M. S. Foster, and P. Kim, Enhanced thermoelectric power in graphene: Violation of the Mott relation by inelastic scattering, *Phys. Rev. Lett.* **116**, 136802 (2016).
- [10] R. Krishna Kumar, D. A. Bandurin, F. M. D. Pellegrino, Y. Cao, A. Principi, H. Guo, G. H. Auton, M. Ben Shalom, L. A. Ponomarenko, G. Falkovich, K. Watanabe, T. Taniguchi, I. V. Grigorieva, L. S. Levitov, M. Polini, and A. K. Geim, Superballistic flow of viscous electron fluid through graphene constrictions, *Nat. Phys.* **13**, 1182 (2017).
- [11] A. I. Berdyugin, S. G. Xu, F. M. D. Pellegrino, R. Krishna Kumar, A. Principi, I. Torre, M. Ben Shalom, T. Taniguchi, K. Watanabe, I. V. Grigorieva, M. Polini, A. K. Geim, and D. A. Bandurin, Measuring Hall viscosity of graphene's electron fluid, *Science* **364**, 162 (2019).
- [12] D. A. Bandurin, A. V. Shytov, L. S. Levitov, R. K. Kumar, A. I. Berdyugin, M. Ben Shalom, I. V. Grigorieva, A. K. Geim, and G. Falkovich, Fluidity onset in graphene, *Nat. Commun.* **9**, 4533 (2018).
- [13] M. J. H. Ku, T. X. Zhou, Q. Li, Y. J. Shin, J. K. Shi, C. Burch, L. E. Anderson, A. T. Pierce, Y. Xie, A. Hamo, U. Vool, H. Zhang, F. Casola, T. Taniguchi, K. Watanabe, M. M. Fogler, P. Kim, A. Yacoby, and R. L. Walsworth, Imaging viscous flow of the Dirac fluid in graphene, *Nature* **583**, 537 (2020).
- [14] J. A. Sulpizio, L. Ella, A. Rozen, J. Birkbeck, D. J. Perello, D. Dutta, M. Ben-Shalom, T. Taniguchi, K. Watanabe, T. Holder, R. Queiroz, A. Principi, A. Stern, T. Scaffidi, A. K. Geim, and S. Ilani, Visualizing Poiseuille flow of hydrodynamic electrons, *Nature* **576**, 75 (2019).
- [15] A. Lucas and K. C. Fong, Hydrodynamics of electrons in graphene, *J. Phys. Condens. Matter* **94**, 2280 (2017).
- [16] B. N. Narozhny, Electronic hydrodynamics in graphene, *Ann. Phys. (N. Y.)* **411**, 167979 (2019).
- [17] H. Guo, E. Ilseven, G. Falkovich, and L. S. Levitov, Higher-than-ballistic conduction of viscous electron flows, *Proc. Natl. Acad. Sci.* **114**, 3068 (2017).
- [18] N. P. Armitage, E. J. Mele, and A. Vishwanath, Weyl and Dirac semimetals in three-dimensional solids, *Rev. Mod. Phys.* **90**, 015001 (2018).
- [19] E. V. Gorbar, V. A. Miransky, I. A. Shovkovy, and P. O. Sukhachov, *Electronic Properties of Dirac and Weyl Semimetals* (World Scientific, 2021).
- [20] J. Gooth, F. Menges, N. Kumar, V. Süß, C. Shekhar, Y. Sun, U. Drechsler, R. Zierold, C. Felser, and B. Gotsmann, Thermal and electrical signatures of a hydrodynamic electron fluid in tungsten diphosphide, *Nat. Commun.* **9**, 4093 (2018).
- [21] U. Vool, A. Hamo, G. Varnavides, Y. Wang, T. X. Zhou, N. Kumar, Y. Dovzhenko, Z. Qiu, C. A. C. Garcia, A. T. Pierce, J. Gooth, P. Anikeeva, C. Felser, P. Narang, and A. Yacoby, Imaging phonon-mediated hydrodynamic flow in WTe₂ with cryogenic quantum magnetometry (2020), arXiv:2009.04477.
- [22] R. Moessner, P. Surówka, and P. Witkowski, Pulsating flow and boundary layers in viscous electronic hydrodynamics, *Phys. Rev. B* **97**, 161112 (2018).
- [23] R. Moessner, N. Morales-Durán, P. Surówka, and P. Witkowski, Boundary-condition and geometry engineering in electronic hydrodynamics, *Phys. Rev. B* **100**, 155115 (2019).
- [24] J. R. Maze, P. L. Stanwix, J. S. Hodges, S. Hong, J. M. Taylor, P. Cappellaro, L. Jiang, M. V. G. Dutt, E. Togan, A. S. Zibrov, A. Yacoby, R. L. Walsworth, and M. D. Lukin, Nanoscale magnetic sensing with an individual electronic spin in diamond, *Nature* **455**, 644 (2008).
- [25] E. V. Levine, M. J. Turner, P. Kehayias, C. A. Hart, N. Langellier, R. Trubko, D. R. Glenn, R. R. Fu, and R. L. Walsworth, Principles and techniques of the quantum diamond microscope, *Nanophotonics* **8**, 1945 (2019).
- [26] P. O. Sukhachov, E. V. Gorbar, and I. A. Shovkovy, Hydrodynamics in Dirac semimetals: Convection impossible (2021), arXiv:2103.15836.
- [27] A. Principi, G. Vignale, M. Carrega, and M. Polini, Bulk and shear viscosities of the two-dimensional electron liquid in a doped graphene sheet, *Phys. Rev. B* **93**, 125410 (2016).
- [28] P. S. Alekseev, Negative magnetoresistance in viscous flow of two-dimensional electrons, *Phys. Rev. Lett.* **117**, 166601 (2016).
- [29] S. A. Hartnoll, P. K. Kovtun, M. Müller, and S. Sachdev, Theory of the Nernst effect near quantum phase transitions in condensed matter and in dyonic black holes, *Phys. Rev. B* **76**, 144502 (2007).
- [30] P. Kovtun and A. Ritz, Universal conductivity and central charges, *Phys. Rev. D* **78**, 066009 (2008).
- [31] S. A. Hartnoll, Theory of universal incoherent metallic transport, *Nat. Phys.* **11**, 54 (2015).
- [32] K. Landsteiner, Y. Liu, and Y.-W. W. Sun, Negative magnetoresistivity in chiral fluids and holography, *J. High Energy Phys.* **2015** (3), 127.
- [33] R. A. Davison, B. Goutéraux, and S. A. Hartnoll, Incoherent transport in clean quantum critical metals, *J. High Energy Phys.* **2015** (10), 112.
- [34] M. S. Shur, *GaAs Devices and Circuits* (Springer US, New York, 1987).
- [35] M. Dyakonov and M. Shur, Shallow water analogy for a ballistic field effect transistor: New mechanism of plasma wave generation by dc current, *Phys. Rev. Lett.* **71**, 2465 (1993).
- [36] L. D. Landau and E. M. Lifshitz, *Fluid Mechanics* (Butterworth-Heinemann, Oxford, 2013).
- [37] E. I. Kiselev and J. Schmalian, Boundary conditions of viscous electron flow, *Phys. Rev. B* **99**, 035430 (2019).
- [38] N. Kumar, Y. Sun, N. Xu, K. Manna, M. Yao, V. Süß, I. Leermakers, O. Young, T. Förster, M. Schmidt, H. Borrmann, B. Yan, U. Zeitler, M. Shi, C. Felser, and C. Shekhar, Extremely high magnetoresistance and conductivity in the type-II Weyl semimetals WP₂ and MoP₂, *Nat. Commun.* **8**, 1642 (2017).
- [39] K. Moors, T. L. Schmidt, and O. Kashuba, Supersonic flow and negative local resistance in hydrodynamic Dirac electron

- nozzles (2019), [arXiv:1905.01247](#).
- [40] L. D. Landau, E. M. Lifshits, and L. P. Pitaevskii, *Electrodynamics of Continuous Media* (Butterworth-Heinemann, Oxford, 1984).
 - [41] J. F. Barry, J. M. Schloss, E. Bauch, M. J. Turner, C. A. Hart, L. M. Pham, and R. L. Walsworth, Sensitivity optimization for NV-diamond magnetometry, *Rev. Mod. Phys.* **92**, 015004 (2020).
 - [42] An oscillating magnetic field attenuates in a conductor with the penetration depth determined by the skin depth. Therefore, even at small magnetic permeability, the gate might distort the time-dependent magnetic field in its vicinity.
 - [43] M. I. Dyakonov and M. S. Shur, Choking of electron flow: A mechanism of current saturation in field-effect transistors, *Phys. Rev. B* **51**, 14341 (1995).